

Full Dynamic-Range Pressure Sensor Matrix Based on Optical and Electrical Dual-Mode Sensing

Xiandi Wang, Miaoling Que, Mengxiao Chen, Xun Han, Xiaoyi Li, Caofeng Pan,* and Zhong Lin Wang*

With a rapid development in mobile network, intelligent terminals including smart wearable equipment, human-machine interactions and artificial electronic skins have attracted more and more attention.^[1] Various industrial products, such as smart bands, glasses, and watches, not only become fashion symbols to extremely enrich our life but also bring convenience to our daily activities.^[2] As an essential component, a pressure sensor with high performance becomes especially urgent to meet the needs of practical applications, and is a new hot area in recent research.^[3] Specially, the pressure sensitivity, detection limits, and measurement range are the key factors for characterizing the general performance of the sensors. The touch screen on the mobile phones, for example, can immediately track the low-pressure contact and map the tactile information at a non-quantitative way. However, few reports are available about a full dynamic-range pressure sensor matrix that can quantify the pressure from kPa to MPa range.

Novel pressure sensors based on different transduction mechanism including piezoresistivity,^[4] capacitance,^[5] and piezoelectricity^[6] have been demonstrated.^[7] These devices exhibit superior performances (Table S1, Supporting Information), but can only work in a limited measurement range.^[8] For many high pressure-sensitive sensors based on piezoresistivity or piezoelectricity, they are over sensitive to a gentle vibration or sound pressure that belongs to the ultralow pressure regimes (<1 Pa).^[9] Meanwhile, it is also easily observed that the measurement range of these devices is relatively small, which is always below 10 kPa. Capacitance-based pressure sensors possess a relatively larger dynamic range (below 100 kPa), but with a lower pressure sensitivity.^[10] Thus, new material systems or sensing mechanisms should be further explored to realize a tunable pressure measurement range and high pressure sensitivity.

Here, we introduce a full dynamic-range pressure sensor matrix (PSM) for mapping pressure distribution with high pressure sensitivity and high resolution, which can basically cover the entire pressure range in our daily life. The PSM composes two sensing components. In low pressure regimes (<100 kPa), a highly sensitive triboelectric sensor matrix (TESM) is designed based on the single-electrode triboelectric nanogenerator, utilizing the coupling effect between contact electrification and electrostatic induction.^[11] Meanwhile, in high pressure regimes (>1 MPa), a mechanoluminescent sensor matrix (MLSM) has advantages in pressure sensitivity, which is based on the mechanoluminescence process.^[12] A 100 × 100 large-scale PSM at a resolution of 100 dpi was demonstrated to detect and rapidly depict the pressure profile in real time by a self-designed image processing system. Pressure sensitivities of 6 and 0.037 MPa⁻¹ were achieved, respectively, corresponding to different working modules in the detection ranges of 0.6–200 kPa and 650 kPa to 30 MPa. In addition, the pressure induced electrical and optical signals are obtained without applying an external electric energy, indicating great potential in achieving self-powered sensing systems.

A schematic of the full dynamic-range high-resolution pressure sensor matrix is shown in **Figure 1a**. The device mainly consists of two parts: a triboelectric sensor matrix and a mechanoluminescent sensor matrix. First, a cross-bar type electrode configuration in the TESM is utilized for the simplification of the device structure and more rapid pressure mapping. Each row and column electrode is composed of aligned rhombuses and these rhombuses are connected along the diagonal directions. Rows of electrode array and columns of electrode array are vertically crossed. An insulating layer is deposited between the horizontal-vertical electrodes to avoid mutual short-circuiting. Scanning electron microscopy (SEM) images of the electrode arrays are shown in **Figure 1b–d**, demonstrating that the rhombic array configuration can obviously enhance the electrode's area ratio in each pixel at a certain resolution, which is a vital parameter for improving the TESM's output voltage.^[13] For a specific example, Ag film of 250 nm thick was used for the electrodes due to its excellent electrical conductivity, which was deposited by magnetron sputtering. An SiO₂ insulating layer about 700 nm thick is employed, deposited by plasma enhanced chemical vapor deposition. With the help of step profiler (KLA Tencor P-7 Profiler), the thickness of each layer was measured and shown in **Figure 1e**. Next, the MLSM consisting of the ZnS:Mn powder and photoresist is fabricated on the top of the electrodes through UV photolithography technique, as illustrated in the inset of **Figure 1a**. Each MLSM pixel center is situated in the middle of the four TESM pixels for more

Dr. X. Wang, M. Que, M. Chen, X. Han, X. Li,
Prof. C. F. Pan, Prof. Z. L. Wang
Beijing Institute of Nanoenergy and Nanosystems
Chinese Academy of Sciences
National Center for Nanoscience and
Technology (NCNST)
Beijing 100083, P. R. China
E-mail: cfpan@binn.cas.cn; zhong.wang@mse.gatech.edu
Prof. Z. L. Wang
School of Materials Science and Engineering
Georgia Institute of Technology
Atlanta, GA 30332-0245, USA



DOI: 10.1002/adma.201605817

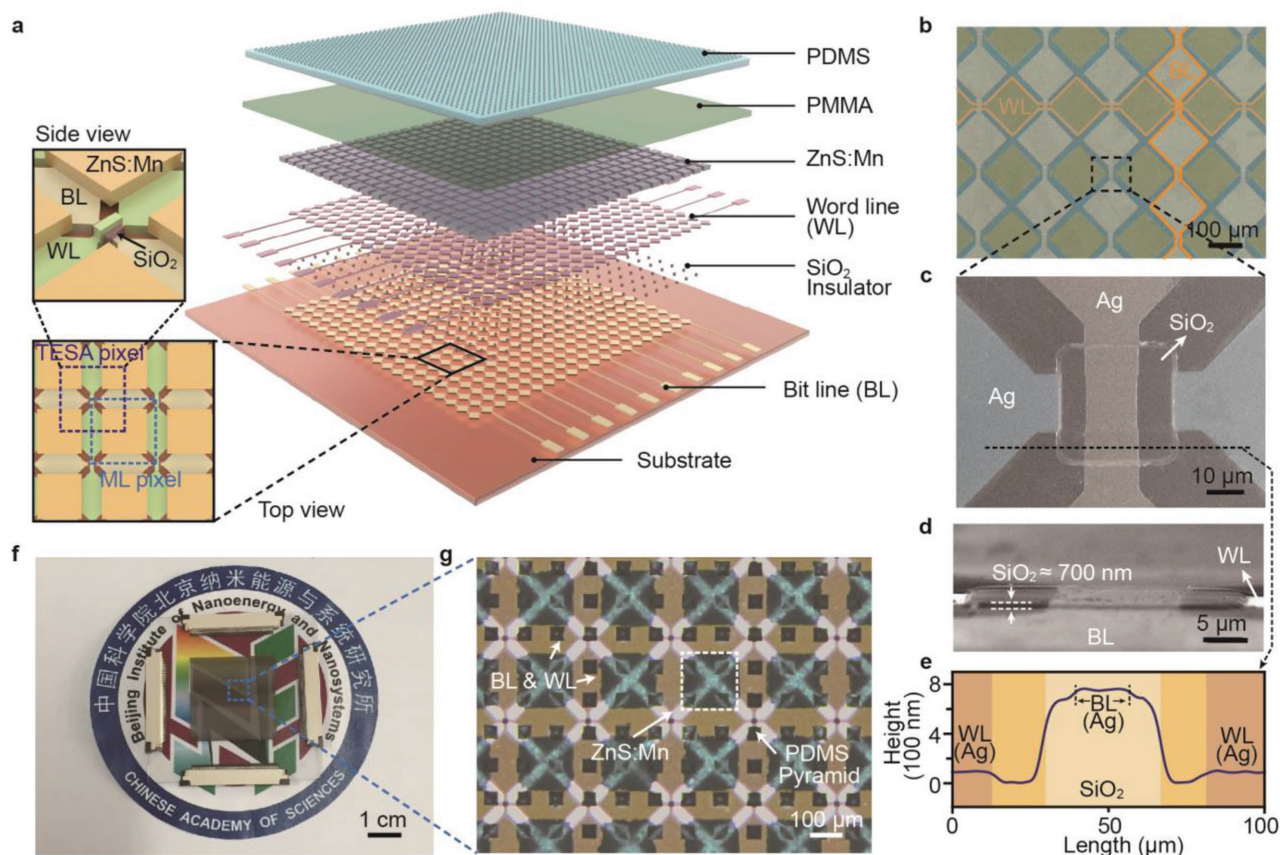


Figure 1. Structure of the full dynamic-range pressure sensor matrix. a) Schematic structure of the device. Insets: the side view and top view of the enlarged structural design, respectively. b,c) SEM image of the electrode arrays of the TESM. d) Cross-sectional SEM image of a single pixel of the TESM. e) Thickness profile of the electrode from the marked area in panel (c). f) Optical photographs of a fully fabricated PSM ($2.54 \times 2.54 \text{ cm}^2$ with a 100×100 pixel matrix). g) Enlarged view of the optical-microscope image.

light penetration. Then, an ultrathin layer of polymethyl methacrylate (PMMA) is spin coated on the surface of the MLSM to prevent it from damaging under pressure. Finally, a prefabricated polydimethylsiloxane (PDMS) film with microstructure on the surface is transferred onto the top of the device, working as the electrification layer of the TESM and generating triboelectric charges after stressing. Actually, other promising candidate materials can also be used as the electrification layer materials, including polyvinyl chloride, polytetrafluoroethylene, and fluorinated ethylene propylene. Figure 1f,g shows optical images of a fully fabricated device, consisting of a 100×100 pixel matrix with an active area of $2.54 \times 2.54 \text{ cm}^2$.

The triboelectric sensor matrix in the PSM device is based on the single-electrode triboelectric nanogenerator. The working principle is coupling effect between contact electrification and electrostatic induction (details can be found in Section B, Figure S1 in the Supporting Information).^[14] In the whole electrical responses, the transferred charge quantity has a significant impact on the output voltage. Especially, the influence of the contact area between the two objects was particularly important according to existing literature, indicating that the increased outputs were obtained with increased contact area.^[15] In addition, the device can convert random mechanical energy into electrical signals without power consumption, that is, the

TESM can spontaneously generate electricity just like a power supply.^[16]

As one of the key components of the TESM, the microstructured elastomer PDMS can effectively improve the transferred charge quantity to obtain different pressure measurement range. PDMS is commonly used in semiconductor device, biomedicine, and artificial electronic skin for its good elastic properties and biocompatibility. And it is a promising electronegativity material with high effective charge density in the process of electrification by friction, especially with the surface modification. This characteristic makes PDMS material a good choice for triboelectric nanogenerator due to its outstanding output performance. In this work, the pressure sensitivity and measurement range of TESM can be effectively adjusted by the different microstructured PDMS thin films, resulting from the elastic deformation under stress, this is, the ability to store and release energy reversibly. Figure 2a shows a schematic process for the fabrication of patterned PDMS films. Si wafer molds with different desired pyramids were first fabricated by traditional photolithography technique and wet etching process (details can be found in Section C, Figures S2 and S3 in the Supporting Information). The SEM images of the Si wafer with 254 pyramids per inch are shown in Figure 2b,c, depicting a uniform and regular inverted pyramid with the 54.7° angle

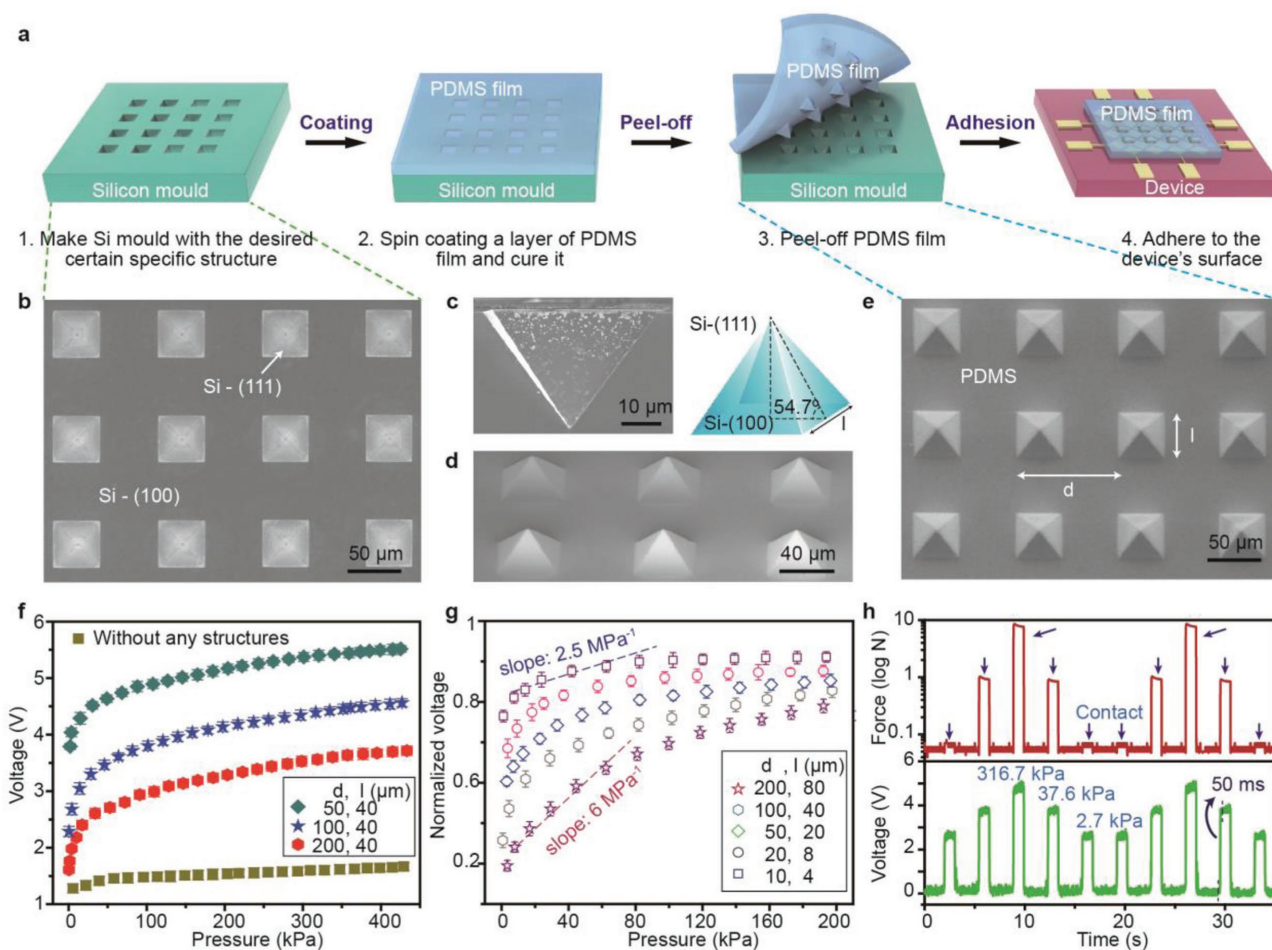


Figure 2. Electrical performance and pressure sensitivity of a TESM. a) Schematic fabrication process of the microstructured PDMS films. b,c) SEM images of the Si mold with regular inverted pyramid by using UV photolithography technique and wet etching process. d,e) SEM images of the PDMS film with pyramid structure lifted off from the Si mold. The pyramid size is $40 \times 40 \mu\text{m}^2$ in area with the height of $28.2 \mu\text{m}$, and the center-to-center distance is $100 \mu\text{m}$. f) Output voltages of the TESM with different types of microstructured PDMS films as a function of pressure. The side length of each pyramid and center-to-center distance are represented symbolically by l and d , respectively (shown in the panel (e)). In these measurements, the devices have the same size of pyramids l but different center-to-center distance d (corresponding densities are 127, 254, and 508 pyramids per inch, respectively). Error bar: one standard deviation. g) Pressure-response curves. The TESM with different size of the pyramid were also investigated in this work, but have the same ratio between l and d , exhibiting different pressure sensitivities from 2.5 to 6 MPa^{-1} . And the bigger the pyramid size is, the larger the measurement range is. The TESM with 127 pyramids per inch show the excellent pressure sensitivity from 0.6 to 200 kPa. h) Pressure responses to various input signals as a function of time, indicating the fine repetition of the TESM. The response time of TESM is 50 ms.

between the slanted plane and square base, which correspond to the Si (111) and Si (100) surface, respectively. Then, the liquid PDMS elastomer (curing agent and polymer are well mixed by weight with a 1:10 ratio) uniformly spin coated on the surface of the Si mold treated primarily with trimethylchlorosilane for the surface activation. After curing, a PDMS film with the inverse pattern features of the mold was obtained by the stripping process, as shown in Figure 2d,e. Finally, the PDMS layer was adhered to the surface of the device by using another thin PDMS bonding layer. For the ability of the device with the tunable pressure range, we accordingly designed different sizes and density of the pyramids in the PDMS film, as illustrated in Figure S4 (Supporting Information).

The pressure response of the TESM with pyramidal microstructured PDMS is shown in Figure 2f-h. Notably, higher output voltage and tunable pressure measurement range were

the two critical factors in this work for the subsequent acquirement of pressure mapping. Initially, Figure 2f shows the output voltages of the TESMs having different PDMS pyramid's densities. It is noteworthy that the device with high density of the pyramid has relatively high voltage output, illustrating that the enhancement of the pyramid's density can improve the output voltage of the sensor. In addition, the pressure sensitivity of these devices remains uniform, indicating that the size of the pyramid is the primary factor that affects pressure sensitivity. Next, the electrical output characteristics of the devices with different sizes of pyramids were further investigated, as shown in Figure 2g. It is easily observed that the pressure sensitivity changes from 2.5 to 6 MPa^{-1} by using different sizes of pyramids, and the bigger the pyramid size is, the larger the measurement range is. The TESM with 127 pyramids per inch shows an excellent pressure sensitivity from 0.6 to 200 kPa.

The pressure response to various input signals for consecutive measurements is illustrated in Figure 2h, indicating the fine repetition of the TESM. What is more, it has fast response time of 50 ms (Section F, Supporting Information). As illustrated above, the TESM is extremely sensitive in low pressure regimes (<100 kPa) and the pressure sensitivity can be adjusted by the pyramidal microstructured PDMS films according to practical application.

The other part of the PSM, mechanoluminescent sensor matrix, is based on the mechanoluminescence process in which visible light can be stimulated by applying pressure. This process is the result of the piezophotonic effect that is a coupling effect between piezoelectricity and photoexcitation.^[12d,17] In this work, ZnS:Mn particles were used for its reproducible luminescence without any physical stimulation like UV irradiation except the applied pressure. The wurtzite structure of ZnS is a noncentral symmetry, resulting in the induction of the

piezoelectric polarization charges under stress. Thereby, the electronic band structure of ZnS is then tilted, and the originally trapped electrons in the impurity states in the bandgap are much easier to be released and make an energy transition. After the process of a nonradioactive recombination and the excited electrons of Mn²⁺ ions fall back to the ground state, a visible light is emitted. It is noteworthy that the whole process does not need any external power except the applied forces.

The synthesis of ZnS:Mn particles with 1 at% Mn²⁺ ions is via a vacuum solid-state reaction by using our previously described methods.^[12d] Figure 3a displays an X-ray powder diffraction (XRD) of the as-synthesized sample, revealing the wurtzite structure of ZnS (JCPDS No. 36-1450). No other diffraction peak is found from the XRD pattern, confirming that there are no manganese compounds in the sample. Transmission electron microscopy (TEM) was carried out to further characterize the crystal structure of the sample. A low-magnification

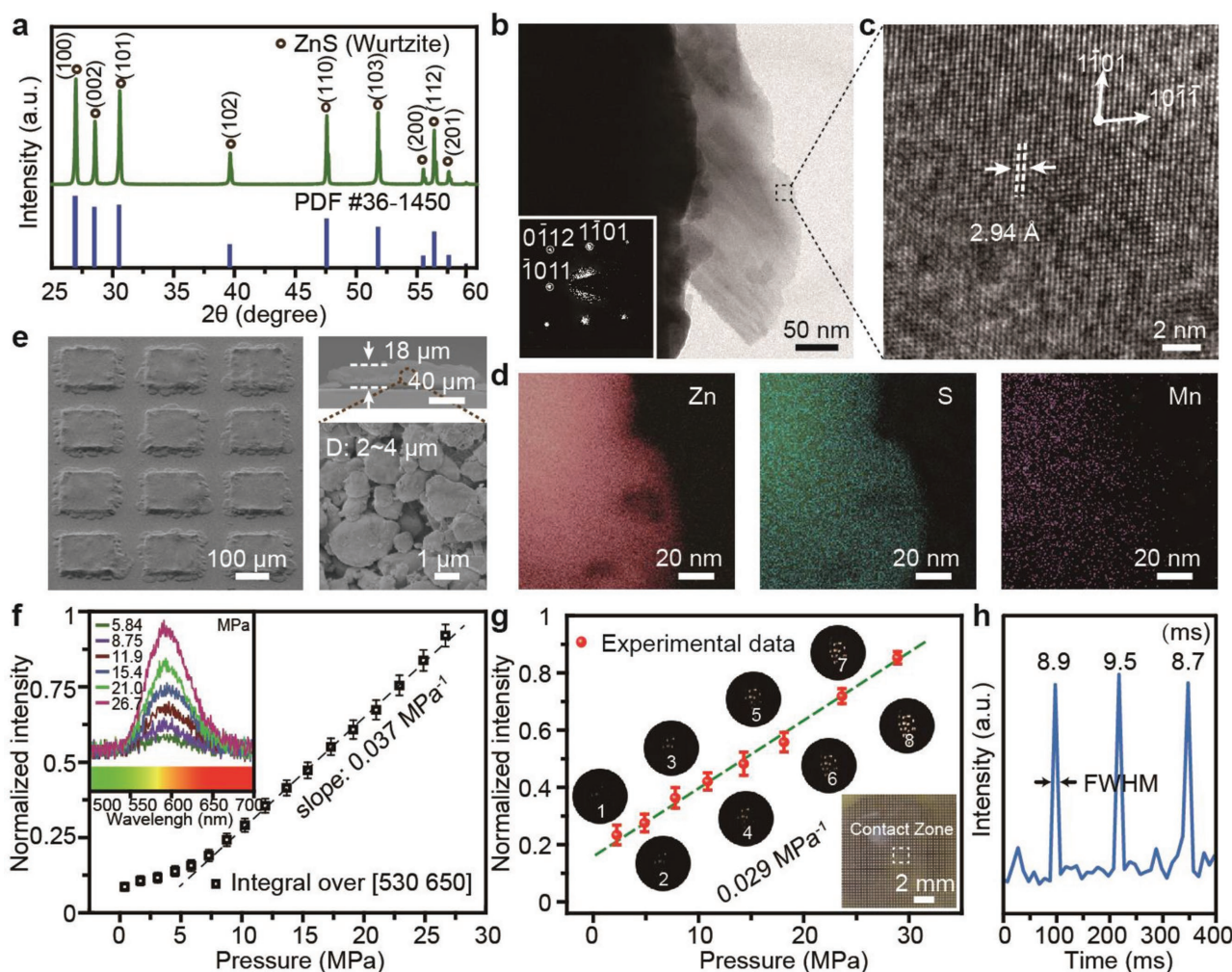


Figure 3. Mechanoluminescence features and pressure sensitivity of the MLSM. a) X-ray diffraction pattern of ZnS powder samples, indicating a typical wurtzite structure (JCPDS No. 36-1450). b) TEM image of the sample. Inset: corresponding SAED pattern. c) HR-TEM image from grain marked in panel (b). d) EDS images corresponding elemental mapping of the Zn, S, and Mn elements, respectively. e) SEM images of the pixels array (consisted of ZnS:Mn particles and photoresist) in the MLSM. Pixel size is $150 \times 150 \mu\text{m}^2$ in area with the height of $18 \mu\text{m}$, and the center-to-center distance is $254 \mu\text{m}$. Lower right corner: SEM image of the ZnS:Mn particles with the size of $2\text{--}4 \mu\text{m}$. f) ML intensity response curves, observing the pressure sensitivities of 0.037 MPa^{-1} . Inset: ML spectra under different applied pressure. g) Gray scale of ML intensity as a function of applied pressure. Inset: collected optical photographs from a CCD camera. h) Response time of MLSM under dynamic pressures mapping test.

bright-field TEM image shows the thinner boundary area, as depicted in Figure 3b. The selected area electron diffraction (SAED) is shown in the inset of Figure 3b, indicating that the gain was the wurtzite crystal structure, taken along the $[01\bar{1}1]$ zone axis. The lattice and interplanar spacing of ZnS (10 $\bar{1}1$) can be clearly observed in the high-resolution TEM (HR-TEM, Figure 3c) image. The energy dispersive spectrum (EDS) analysis was adopted to investigate the elementary composition, as shown in Figure 3d, indicating that the product is rich in Zn and S, while Mn is relatively low without any agglomeration. Based on the above analysis, it is confirmed that the product of ZnS:Mn is fine crystalline with the wurtzite crystal structure. Finally, a high-resolution MLSM with the mixture of ZnS:Mn and photoresist arrays can be fabricated by using UV photolithography technique. SEM images (Figure 3e) clearly show the well-aligned pixels of MLSM with the size of $150 \times 150 \mu\text{m}^2$ and the height of $18 \mu\text{m}$.

The pressure sensitivity and measurement range of the MLSM were carefully investigated. When the MLSM is under different pressure, the corresponding ML spectrum can be observed, as shown in the inset of Figure 3f, which has a common peak near 590 nm among the emission range of 530–650 nm. The integral intensity over 530–650 nm of these spectra as a function of each loaded pressure condition are summarized in Figure 3f, indicating that emission intensity

increases with the applied pressure. After a standard calibration, the pressure sensitivity of the MLSM is about 0.037 MPa^{-1} with the measurement range from 650 kPa to 30 MPa, which is defined as the slope of ML intensity curve. Instead of the spectrograph, a charge-coupled device (CCD) was employed to obtain visible-light optical images. By extracting the gray values of the acquired images, a similar linear relationship between the gray value of ML intensity and pressure is clearly observed after a standard calibration (the slope is 0.029 MPa^{-1}), as shown in Figure 3g. Response and relaxation time constants were characterized by full width at half-maximum (FWHM) of ML intensity. The statistic result of FWHM from 100 peaks shows a mean value of $9.23 \pm 0.54 \text{ ms}$ (97.5% confidence interval). A small part of the ML curve is shown in Figure 3h (details can be found in Section F in the Supporting Information). This result indicates that the device has a fast and deterministic response, meaning that significant information will be gained faster by using optical signal, even if the measured time constants are limited by our spectrometer's time resolution. Notably, the MLSM is greatly sensitive in high pressure regimes ($>1 \text{ MPa}$) and the different intensity of emitted yellow light provides a new way to sense pressure directly by eyes.

Figure 4a shows a schematic illustration of how the PSM works and the diverse potential applications corresponding to the pressure range. When a smaller pressure is applied, the

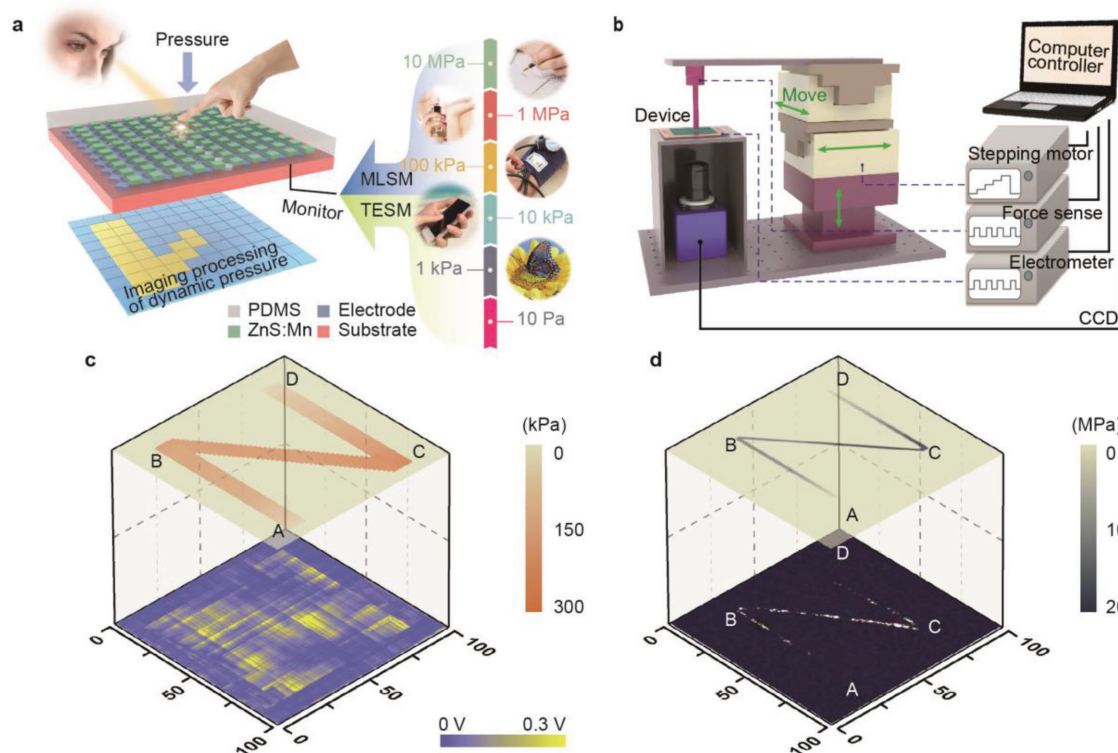


Figure 4. Performance of the integrated PSM for pressure mapping. a) Illustration of the pressure mapping process. Right: diagram of pressure regimes and the relevant applications in our daily life. The TESM is highly sensitive in low pressure regimes ($<500 \text{ kPa}$) and the MLSM is extremely sensitive in high pressure regimes ($>1 \text{ MPa}$). b) Schematic diagram of measurement system for dynamic pressure mapping. The stepping motor and dynamometer are employed to provide the monitoring of 3D dynamic stress. A CCD and electrometer are used to collect the optical and electrical signal from the device. Pressure mapping is available by using a self-developed computer software. c) Electrical output voltage of the PSM in low pressure regimes. Top: 3D pressure distribution acquired from the home-developed software. Bottom: output voltage distribution observed from the PSM. d) Optical signal of the PSM in high pressure regimes from a CCD camera. The path: A \rightarrow B \rightarrow C \rightarrow D.

TESM makes a significant contribution to the success of pressure mapping, of which the output voltage is collected by a home-developed software to analyze and rebuild the tactile and pressure information. On the other hand, when the PSM is under a larger pressure, the ML intensity of the MLSM is more sensitive to the change in pressure although the electric and optical signals can be obtained at the same time. Notably, the electrical readout and optical visualization can be performed by monitoring the voltage and light intensity of each pixel, and play a replaceable role in different pressure regimes.

A schematic diagram of the measurement system for dynamic pressure mapping is shown in Figure 4b. A stepping motor with 3D translation and a force sensor are utilized to monitor the pressure distribution between the contact object and the device. The movement of the stepping motor in the Z-axis direction will change the pressure between the two objects in contact, while it will supply the tactile information along the X-, Y-axis directions. A CCD and an electrometer are employed to acquire the optical and electrical signal from the device under stress. All these measurement equipment are controlled by a computer with home-developed software to complete the image processing.

The experimental mappings at different pressures are illustrated in Figure 4c,d. The program controlled movement track was an "N" shape (point A → B → C → D), and different sizes of the contact objects were performed to obtain different pressure regimes. The actual pressure distribution is shown in the top of Figure 4c,d, illustrating that the pressure increases from point A to point C and then began a precipitous decline. Figure 4c shows the electrical readout of the PSM in low pressure regimes, which is consistent with the actual pressure distribution excluding some signal crosstalk. And Figure 4d presents the visible image from a CCD, indicating that the maximum light intensity occurred in the point C but almost no light was observed at the beginning and ending part in the process due to small pressure.

The full dynamic-range PSM is suitable for monitoring pressure distribution in our daily life, which is promising to achieve a wide range of applications in human-machine interfacing, health monitoring, and intelligent electronic skin. Nowadays, various pressure sensors based on different transduction mechanism are developed. Different from what have been reported in literature, a full dynamic-range PSM with two different modules (TESM and MLSM) make it possible to provide a pressure mapping no matter it is in low pressure regimes or in high pressure regimes. Moreover, the device has a fast response time, which is 50 and 9.23 ms in the TESP and MLSM modules, respectively (details can be found in Section F in the Supporting Information). Obviously, the 100 × 100 large-scale PSM at a resolution of 100 dpi is high resolution compared with other pressure sensors (Table S1, Supporting Information). However, the electric or optical signals will attenuate when the pixel size further reduces. So, small signal processing components like amplifying circuit can be considered to be employed to improve the resolution of the device in future work.

To conclude, we have developed a full dynamic-range pressure sensor matrix for the visualization of pressure distribution no matter it is in low pressure regimes (<100 kPa) or in

high pressure regimes (>1 MPa) in our daily life. The device was integrated with two sensing components, a TESP based on the single-electrode triboelectric nanogenerator and an MLSM based on the mechanoluminescence process, which can acquire electrical and optical signals without an external power source. A 100 × 100 large-scale PSM at a resolution of 100 dpi has excellent pressure sensitivity, which is 6 MPa⁻¹ from 0.6 to 200 kPa and 0.037 MPa⁻¹ from 650 kPa to 30 MPa. This is the first demonstration of a pressure sensor with large measurement range that can not only monitors and spatially maps the pressure distribution in real time with the assistance of image processing by a program but also enables the pressure profile to be visible due to the response of emission light. We predict that the presented device may achieve a wide range of applications in health monitoring, robotics, human-machine interfacing, and intelligent electronic skin.

Experimental Section

Fabrication of the PSM: For the fabrication of the PSM, a 5 × 5 cm² glass substrate was employed. 250 nm thick Ag electrodes and 700 nm thick SiO₂ were then successively deposited by magnetron sputtering (PVD75 Kurt J. Lesker) and plasma enhanced chemical vapor deposition (SI 500D SENTECH), respectively, which were defined by photolithography and lift-off. Next, the mixture of ZnS:Mn and photoresist arrays were fabricated on the top of the electrodes through UV photolithography technique (MA6 SUSS). The ZnS:Mn practices were synthesized by a vacuum solid-state reaction, as described in the previous work by Wang et al.^[12d] Subsequently, an ultrathin layer of PMMA (A4, NIPPON KAYAKU CO. LTD) was spin coated on the device. Finally, a PDMS film (SYLGARD184 Dowcorning) with pyramid structure was transferred onto the surface of device (details can be found in Sections C and D in the Supporting Information).

Materials Characterization: The crystallization of the powders was characterized by X-ray diffraction (X'Pert3 Powder) θ - 2θ scan with Cu K radiation. Conventional TEM, high-resolution TEM, and selected area electron diffraction measurements (Tecnai G2 F20, FEI) were carried out to determine the shape, size, and crystallinity of the as-synthesized ZnS:Mn. The field-emission scanning electron microscopy (SU8020 Hitachi) was employed to characterize the morphologies of the samples.

Measurement Setup: A home-made measuring system was built to collect electric and optical signals when the device was under applied force. A stepping motor (XPS Controller Newport) consisted of three independent single-axis motion modules can realize the periodical contact/separation motion or 3D movement. The contact pressure was measured by a pressure sensor (Nano17 ATI) which is tied to the stepping motor. A high-impedance electrometer (Keithley 6514) was used to measure the output voltage and a spectrometer (QE65pro Ocean Optics) in the range of 200–900 nm was carried out to analyze the spectral curve of the emission light in the ML process. For the image processing of the pressure distribution, a self-developed Labview program was used to precisely control the movement of contact objects and accurately monitor the optical and electrical signals from the device. Instead of the Keithley 6514, a digital multimeter (PXI-4072 National Instruments) with scanning matrix switches (PXI-2530, PXI-2630B, National Instruments) was employed for the electrical measurements of the array device due to the rapid addressing speed.

Supporting Information

Supporting Information is available from the Wiley Online Library or from the author.

Acknowledgements

X.W. and M.Q. contributed equally to this work. The authors are thankful for support from the “Thousand Talents” program of China for pioneering researchers and innovative teams, the support of national key R & D project from Minister of Science and Technology, China (Grant No. 2016YFA0202703), National Natural Science Foundation of China (Grant Nos. 51622205, 61675027, 61405040, 51432005, 61505010, and 51502018), Beijing City Committee of Science and Technology (Grant No. Z151100003315010), Beijing Natural Science Foundation (Grant No. 2164076), the President Funding of the Chinese Academy of Sciences, and the China Postdoctoral Science Foundation Funded Project (Grant Nos. BX201600040 and 2016M600976).

Received: October 29, 2016

Revised: November 19, 2016

Published online: January 6, 2017

- [1] a) M. L. Hammock, A. Chortos, B. C. K. Tee, J. B. H. Tok, Z. Bao, *Adv. Mater.* **2013**, 25, 5997; b) X. Wang, L. Dong, H. Zhang, R. Yu, C. Pan, Z. L. Wang, *Adv. Sci.* **2015**, 2, 1500169; c) C. Larson, B. Peele, S. Li, S. Robinson, M. Totaro, L. Beccai, B. Mazzolai, R. Shepherd, *Science* **2016**, 351, 1071.
- [2] a) L. M. Huang, C. W. Hu, H. C. Liu, C. Y. Hsu, C. H. Chen, K. C. Ho, *Sol. Energy Mater. Sol. Cells* **2012**, 99, 154; b) W. Gao, S. Emaminejad, H. Y. Y. Nyein, S. Challa, K. V. Chen, A. Peck, H. M. Fahad, H. Ota, H. Shiraki, D. Kiriya, D. H. Lien, G. A. Brooks, R. W. Davis, A. Javey, *Nature* **2016**, 529, 509.
- [3] a) B. W. Zhu, H. Wang, Y. Q. Liu, D. P. Qi, Z. Y. Liu, H. Wang, J. C. Yu, M. Sherburne, Z. H. Wang, X. D. Chen, *Adv. Mater.* **2016**, 28, 1559; b) S. Xu, Y. Zhang, L. Jia, K. E. Mathewson, K.-I. Jang, J. Kim, H. Fu, X. Huang, P. Chava, R. Wang, S. Bhole, L. Wang, Y. J. Na, Y. Guan, M. Flavin, Z. Han, Y. Huang, J. A. Rogers, *Science* **2014**, 344, 70.
- [4] a) C. Pang, G.-Y. Lee, T.-I. Kim, S. M. Kim, H. N. Kim, S.-H. Ahn, K.-Y. Suh, *Nat. Mater.* **2012**, 11, 795; b) L. Pan, A. Chortos, G. Yu, Y. Wang, S. Isaacson, R. Allen, Y. Shi, R. Dauskardt, Z. Bao, *Nat. Commun.* **2014**, 5, 3002.
- [5] a) D. J. Lipomi, M. Vosgueritchian, B. C. K. Tee, S. L. Hellstrom, J. A. Lee, C. H. Fox, Z. Bao, *Nat. Nanotechnol.* **2011**, 6, 788; b) K. Takei, T. Takahashi, J. C. Ho, H. Ko, A. G. Gillies, P. W. Leu, R. S. Fearing, A. Javey, *Nat. Mater.* **2010**, 9, 821.
- [6] a) W. Wu, X. Wen, Z. L. Wang, *Science* **2013**, 340, 952; b) C. Pan, L. Dong, G. Zhu, S. Niu, R. Yu, Q. Yang, Y. Liu, Z. L. Wang, *Nat. Photonics* **2013**, 7, 752.
- [7] a) T. Sekitani, T. Yokota, U. Zschieschang, H. Klauk, S. Bauer, K. Takeuchi, M. Takamiya, T. Sakurai, T. Someya, *Science* **2009**, 326, 1516; b) D.-H. Kim, N. Lu, R. Ma, Y.-S. Kim, R.-H. Kim, S. Wang, J. Wu, S. M. Won, H. Tao, A. Islam, K. J. Yu, T.-I. Kim, R. Chowdhury, M. Ying, L. Xu, M. Li, H.-J. Chung, H. Keum, M. McCormick, P. Liu, Y.-W. Zhang, F. G. Omenetto, Y. Huang, T. Coleman, J. A. Rogers, *Science* **2011**, 333, 838; c) T. Someya, T. Sekitani, S. Iba, Y. Kato, H. Kawaguchi, T. Sakurai, *Proc. Natl. Acad. Sci. USA* **2004**, 101, 9966; d) C. F. Pan, Z. X. Luo, C. Xu, J. Luo, R. R. Liang, G. Zhu, W. Z. Wu, W. X. Guo, X. X. Yan, J. Xu, Z. L. Wang, J. Zhu, *ACS Nano* **2011**, 5, 6629; e) C. F. Pan, W. X. Guo, L. Dong, G. Zhu, Z. L. Wang, *Adv. Mater.* **2012**, 24, 3356; f) W. X. Guo, C. Xu, G. Zhu, C. F. Pan, C. J. Lin, Z. L. Wang, *Nano Energy* **2012**, 1, 176; g) F. Zhang, X. H. Liu, C. F. Pan, J. Zhu, *Nanotechnology* **2007**, 18, 345302.
- [8] a) C. Wang, D. Hwang, Z. Yu, K. Takei, J. Park, T. Chen, B. Ma, A. Javey, *Nat. Mater.* **2013**, 12, 899; b) T. Sekitani, U. Zschieschang, H. Klauk, T. Someya, *Nat. Mater.* **2010**, 9, 1015.
- [9] a) Y. Zhang, F. Zhang, D. Huang, X. Gao, C.-A. Di, D. Zhu, *Nat. Commun.* **2015**, 6, 6269; b) M. Kaltenbrunner, T. Sekitani, J. Reeder, T. Yokota, K. Kuribara, T. Tokuhara, M. Drack, R. Schwoedlauer, I. Graz, S. Bauer-Gogonea, S. Bauer, T. Someya, *Nature* **2013**, 499, 458; c) D. Kang, P. V. Pikhitsa, Y. W. Choi, C. Lee, S. S. Shin, L. Piao, B. Park, K.-Y. Suh, T.-I. Kim, M. Choi, *Nature* **2014**, 516, 222.
- [10] a) S. Y. Kim, S. Park, H. W. Park, D. H. Park, Y. Jeong, D. H. Kim, *Adv. Mater.* **2015**, 27, 4178; b) X. Han, W. M. Du, R. M. Yu, C. F. Pan, Z. L. Wang, *Adv. Mater.* **2015**, 27, 7963; c) X. Y. Li, M. X. Chen, R. M. Yu, T. P. Zhang, D. S. Song, R. R. Liang, Q. L. Zhang, S. B. Cheng, L. Dong, A. L. Pan, Z. L. Wang, J. Zhu, C. F. Pan, *Adv. Mater.* **2015**, 27, 4447.
- [11] a) F. R. Fan, L. Lin, G. Zhu, W. Wu, R. Zhang, Z. L. Wang, *Nano Lett.* **2012**, 12, 3109; b) F. R. Fan, Z. Q. Tian, Z. Lin Wang, *Nano Energy* **2012**, 1, 328; c) G. Zhu, W. Q. Yang, T. Zhang, Q. Jing, J. Chen, Y. S. Zhou, P. Bai, Z. L. Wang, *Nano Lett.* **2014**, 14, 3208; d) W. Du, X. Han, L. Lin, M. Chen, X. Li, C. Pan, Z. L. Wang, *Adv. Energy Mater.* **2014**, 4, 1301592; e) M. Chen, X. Li, L. Lin, W. Du, X. Han, J. Zhu, C. Pan, Z. L. Wang, *Adv. Funct. Mater.* **2014**, 24, 5059.
- [12] a) C. N. Xu, T. Watanabe, M. Akiyama, X. G. Zheng, *Appl. Phys. Lett.* **1999**, 74, 1236; b) S. M. Jeong, S. Song, S. K. Lee, N. Y. Ha, *Adv. Mater.* **2013**, 25, 6194; c) S. M. Jeong, S. Song, K.-I. Joo, J. Kim, S.-H. Hwang, J. Jeong, H. Kim, *Energy Environ. Sci.* **2014**, 7, 3338; d) X. Wang, H. Zhang, R. Yu, L. Dong, D. Peng, A. Zhang, Y. Zhang, H. Liu, C. Pan, Z. L. Wang, *Adv. Mater.* **2015**, 27, 2324; e) L. Chen, M. C. Wong, G. X. Bai, W. J. Jie, J. H. Hao, *Nano Energy* **2015**, 14, 372; f) Y. Zhang, G. Y. Gao, H. L. W. Chan, J. Y. Dai, Y. Wang, J. H. Hao, *Adv. Mater.* **2012**, 24, 1729.
- [13] X. Wang, H. Zhang, L. Dong, X. Han, W. Du, J. Zhai, C. Pan, Z. L. Wang, *Adv. Mater.* **2016**, 28, 2896.
- [14] a) L. Lin, Y. Xie, S. Wang, W. Wu, S. Niu, X. Wen, Z. L. Wang, *ACS Nano* **2013**, 7, 8266; b) W. Yang, J. Chen, X. Wen, Q. Jing, J. Yang, Y. Su, G. Zhu, W. Wu, Z. L. Wang, *ACS Appl. Mater. Interfaces* **2014**, 6, 7479; c) F. Yi, L. Lin, S. Niu, J. Yang, W. Wu, S. Wang, Q. Liao, Y. Zhang, Z. L. Wang, *Adv. Funct. Mater.* **2014**, 24, 7488.
- [15] S. M. Niu, S. H. Wang, L. Lin, Y. Liu, Y. S. Zhou, Y. F. Hu, Z. L. Wang, *Energy Environ. Sci.* **2013**, 6, 3576.
- [16] S. Wang, L. Lin, Z. L. Wang, *Nano Energy* **2015**, 11, 436.
- [17] a) Z. L. Wang, *Adv. Funct. Mater.* **2008**, 18, 3553; b) Z. L. Wang, *Nano Today* **2010**, 5, 540; c) L. B. Huang, G. X. Bai, M. C. Wong, Z. B. Yang, W. Xu, J. H. Hao, *Adv. Mater.* **2016**, 28, 2744; d) M. C. Wong, L. Chen, M. K. Tsang, Y. Zhang, J. H. Hao, *Adv. Mater.* **2015**, 27, 4488; e) L. Dong, S. M. Niu, C. F. Pan, R. M. Yu, Y. Zhang, Z. L. Wang, *Adv. Mater.* **2012**, 24, 5470.